



***Dedicated to  
My Beloved Family***



## CERTIFICATE

It is certified that the work contained in the thesis entitled "**DISCOVERY OF NEW LOW TEMPERATURE PHASE TRANSITIONS IN BARIUM HEXAFERRITE**" by "**KESHAV KUMAR**" has been carried out under my supervision and that this work has not been submitted elsewhere for a degree.

It is further certified that the student has fulfilled all the requirements of Comprehensive, Candidacy and SOTA for the award of Ph.D. degree.

Date: 19.01.2021

Place: Varanasi




**Prof. Dhananjai Pandey**  
(Supervisor)  
School of Materials Science & Technology  
Indian Institute of Technology  
(Banaras Hindu University)  
Varanasi  
Institute Professor/संस्थान आचार्य  
School of Materials Science & Technology/पदार्थ विज्ञान एवं प्रौद्योगिकी स्कूल  
Indian Institute of Technology/भारतीय प्रौद्योगिकी संस्थान  
(Banaras Hindu University), Varanasi/काशी हिन्दू विश्वविद्यालय, वाराणसी



## DECLARATION BY THE CANDIDATE

I, **KESHAV KUMAR**, certify that the work embodied in this Ph.D. thesis is my own bonafide work carried out by me under the supervision of **PROF. DHANANJAI PANDEY** for a period from **JULY 2014** to **DECEMBER 2020** at the **SCHOOL OF MATERIALS SCIENCE AND TECHNOLOGY**, Indian Institute of Technology (BHU), Varanasi. The matter embodied in this Ph.D. thesis has not been submitted for the award of any other degree/diploma. I declare that I have faithfully acknowledged and given credits to the research workers wherever their works have been cited in my work in this thesis. I further declare that I have not will fully copied any other's work, paragraphs, text, data, results, *etc.*, reported in journals, books, magazines, reports, dissertations, thesis, *etc.*, or available at websites and have not included them in this thesis and have not cited as my own work.

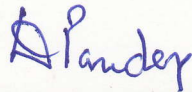
Date: 19.01.2021

  
(Keshav Kumar)

Place: Varanasi

## CERTIFICATE BY THE SUPERVISOR

This is to certify that the above statement made by the candidate is correct to the best of my knowledge.



**Prof. Dhananjai Pandey**  
(Supervisor)

**School of Materials Science & Technology**  
**Indian Institute of Technology**  
(Banaras Hindu University)  
Varanasi

**Institute Professor/संस्थान आचार्य**

**School of Materials Science & Technology/पदार्थ विज्ञान एवं प्रौद्योगिकी स्कूल**  
**Indian Institute of Technology/भारतीय प्रौद्योगिकी संस्थान**  
(Banaras Hindu University), Varanasi/काशी हिन्दू विश्वविद्यालय, वाराणसी



**Dr. Chandana Rath**  
(Coordinator)

**School of Materials Science & Technology**  
**Indian Institute of Technology**  
(Banaras Hindu University)  
Varanasi

**Coordinator/समन्वयक**

**School of Materials Science & Technology/पदार्थ विज्ञान एवं प्रौद्योगिकी स्कूल**  
**Indian Institute of Technology/भारतीय प्रौद्योगिकी संस्थान**  
(Banaras Hindu University), Varanasi/काशी हिन्दू विश्वविद्यालय, वाराणसी



## COPYRIGHT TRANSFER CERTIFICATE

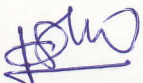
Title of the Thesis: "*Discovery of New Low Temperature Phase Transitions in Barium Hexaferrite*"

Candidate's Name: Mr. Keshav Kumar

### Copyright Transfer

The undersigned hereby assigns to the Indian Institute of Technology (Banaras Hindu University), Varanasi all rights under copyright that may exist in and for the above thesis submitted for the award of the *Doctor of Philosophy*.

Date: 19.01.2021

  
(Keshav Kumar)

Place: Varanasi

**Note:** However, the author may reproduce or authorize others to reproduce materials extracted verbatim from the thesis or derivative of the thesis for author's personal use provided that the source and the Institute's copyright notice are indicated.





## Acknowledgements

*First and Foremost, I wish to express my sincere gratitude to my esteemed supervisor, Prof. Dhananjai Pandey, for his guidance, support and valuable suggestions throughout my Ph.D. work. His constant monitoring and interest in my work over the last six years will always remain as a happy memory. His patience and enthusiastic approach for my training in the field of crystallography, multiferroics, spin-glass, dipole glass, structural phase transition and quantum phase transitions cannot be expressed in words and I will always remain thankful to him.*

*I would also like to express my gratitude towards the faculty members of the School of materials Science and Technology, Prof. R. Prakash, Prof. P. Maiti, Dr. (Mrs) C. Rath (Coordinator), Dr. A. K. Singh, Dr. C. Upadhyay, Dr. A. K. Mishra, Dr. S. K. Mishra, and Dr. S. Singh (DPGC convener), Dr. S. R. Singh, Prof. J. Kumar, Dr. Ashish Singh for providing constant encouragement and invaluable suggestions during my Ph.D. work which greatly helped me to complete my work with confidence.*

*I am thankful to Department of Science and Technology (DST), Government of India for financial support to carry out (1) XAS/XMCD measurements at Petra III, Hamburg, Germany and (2) Single-crystal neutron diffraction measurements using WISH diffractometer at ISIS-RAL, Didcot, UK.*

*I am very grateful to Dr. P. Manuel, Dr. F. Orlandi and Dr. S. Singh for their helping hands and valuable suggestions during measurements and analysis of single-crystal neutron diffraction data.*

*I am also very grateful to Dr. M. Martins, Dr. I. Baev and Dr. S. K. Mishra for their helping hands and valuable suggestions during measurements and analysis of XAS and XMCD data.*

*I am thankful to Dr. A. Senyshyn, FRM II, Garching Germany, for providing powder neutron diffraction data.*

*I am also very thankful to my external RPEC member Dr. Preetam Singh (Ceramic Eng., IIT BHU), for their valuable suggestions and help during my PhD work.*

*I would like to express my extreme gratefulness towards my seniors; Dr. A. Singh, Dr. S. Bhattacharjee, Late Dr. R. S. Solanki, Dr. S. Tripathi, Dr. J. P. Patel, Dr. Pappu Kumar, Dr. V. Tiwari, Dr. D. K. Patel, Dr. A. Upadhyay, Dr. A. Mahanta, Dr. Madhu, Dr. S. Pandey, Dr. S. Kumar, Dr. Arun. Kumar, Dr. Narendra, Dr. Arpan, Dr. Preeti, Dr. Pinki and Dr. Chandrabhal for helping me during whole period of my Ph.D. work, whenever I needed.*

*Words fail to express my earnest thanks to all my friends: Pramod, Praveen Shahi, Abhishek Dwedy, Prince Gupta, Abhishek Yadav, Satyaveer, Aravintha, Bharti,*

*Kirti Bind, Richa, Girish, Nirmal, Vinay, for giving me moral support, pleasant company and confidence to complete my work with a 'smile'.*

*I am also thankful to all my juniors: Pragya, Dipti, Majari, Monika, Nitesh, Anupam, Amit, Deepti, Pragyanand, Bisnu, Shyam Babu, Gaurav Chandra, Manish, Krishna Kant, Raman, Nisha, Gaurav, Ishita, Aditya, Vikas, Payal and Vishal for providing pleasant, encouraging and friendly environment.*

*I am also very thankful to technical and non-technical staff of my school: Mr. Amarnath, Ambresh Rai, Kallu Ram, Ashwani, Sitaram Tiwari, Samir Dubey, Mahendra, Dharmendra, Waris, Awanish, Ankit, Sudhakar, Dinesh, Sajan and Jaislaal for the cooperation and help. Special thanks to Mr. Amod Kumar Pandey and Kumar bhaiya for the help throughout my PhD work.*

*I would like to express my heart-felt gratitude towards my grandfather Late Shri Baijnath Bind and mother Smt. Usha Devi for their constant encouragements, moral support and blessing at every step of my life cannot be expressed in words. My special thanks are due to my younger sister Ms. Geeta Bind and brothers Mr. Kapil Dev and Mr. Vedpraksh for his love and affection. My love and wishes are always with them.*

*Finally, I thank **GOD** for giving me strength to complete my thesis successfully.*

Date: 19.01.2021

(Keshav Kumar)

Place: Varanasi

## Table of Contents

<b>Acknowledgements .....</b>	<b>i</b>
<b>Table of Contents .....</b>	<b>iii</b>
<b>List of Figures.....</b>	<b>vii</b>
<b>List of Tables .....</b>	<b>xxiii</b>
<b>List of Abbreviations .....</b>	<b>xxv</b>
<b>List of Symbols .....</b>	<b>xxvii</b>
<b>Preface.....</b>	<b>xxxi</b>
<b>Chapter 1      Introduction and Literature Review .....</b>	<b>1</b>
1.1      Introduction.....	1
1.2      Ferroics .....	1
1.3      Ferromagnetism .....	2
1.4      Antiferromagnetism and Ferrimagnetism .....	3
1.5      Ferroelectricity .....	5
1.6      Antiferroelectricity and Ferrielectricity .....	6
1.7      Quantum Paraelectrics .....	7
1.8      Spin-Glasses, Dipole glasses and Relaxors .....	9
1.9      Multiferroics .....	14
1.10     The Hexaferrites.....	15
1.10.1    Crystal Structure .....	15
1.10.2    Multiferroicity in Hexaferrites .....	19
1.10.3    Technological Applications of Hexaferrites .....	23
1.11     Recent Advances in M-type Hexaferrites .....	24
1.12     Objectives of the Present Work .....	33
<b>Chapter 2      Synthesis of Polycrystalline and Single-Crystal Growth of BaFe<sub>12</sub>O<sub>19</sub> .....</b>	<b>35</b>
2.1      Introduction.....	35
2.2      Experimental .....	36
2.3      Synthesis of BaFe <sub>12</sub> O <sub>19</sub> Polycrystalline Samples .....	36
2.3.1    Optimization of Calcination Temperature .....	37

2.3.2	Optimization of Sintering Temperature .....	38
2.4	Details of Crystal Growth of BaFe <sub>12</sub> O <sub>19</sub> .....	39
2.4.1	Crystallinity and Phase Purity of Single Crystals .....	39
2.4.2	Chemical Composition of Single Crystals .....	41
2.4.3	Iodometry Titration .....	42
2.5	Room Temperature Crystal Structure of BaFe <sub>12</sub> O <sub>19</sub> .....	43
2.6	Conclusions .....	47
<b>Chapter 3</b>	<b>Magnetic Ground State of BaFe<sub>12</sub>O<sub>19</sub>: Evidence for Noncollinear Magnetic Structure and Incommensurate Conical Modulation.....</b>	<b>49</b>
3.1	Introduction .....	49
3.2	Current Understanding of the XAS Spectra at the Fe L <sub>2,3</sub> -edges.....	51
3.3	Current Understanding of X-ray Magnetic Circular Dichroism (XMCD) at the Fe L <sub>2,3</sub> -edges .....	54
3.4	Experimental .....	59
3.5	Results and Discussion .....	60
3.5.1	XAS and XMCD Study at the Fe L <sub>2,3</sub> -edges at 1.2 K.....	60
3.5.2	Neutron Diffraction Study at 1.5 K.....	68
3.6	Conclusions .....	71
<b>Chapter 4</b>	<b>Evidence for Spin Canting in BaFe<sub>12</sub>FO<sub>19</sub> at T &gt; 1.5 K .....</b>	<b>73</b>
4.1	Introduction .....	73
4.2	Experimental .....	74
4.3	Results and Discussion .....	75
4.3.1	DC Magnetization Studies .....	75
4.3.2	XAS and XMCD Studies at the Fe L <sub>2,3</sub> -edges from 1.2 to 30 K .....	79
4.3.3	Variation of the Magnetic Moment obtained from XMCD and dc Magnetization Measurements with Temperature.....	84
4.3.4	XAS Studies at the Oxygen (O) K-edge .....	88
4.3.4.1	XAS Study at Oxygen K-edge at 1.2 K.....	88
4.3.4.2	XAS Spectra at the Oxygen K-edge as a Function of Temperature.....	91
4.4	Conclusions.....	94
<b>Chapter 5</b>	<b>Evidence for Four Spin-Glass Transitions in BaFe<sub>12</sub>O<sub>19</sub> due to Successive Freezing of Transverse and Longitudinal Spin Components .....</b>	<b>101</b>
5.1	Introduction.....	101
5.2	Experimental .....	103

5.3	Magnetic Susceptibility Studies.....	104
5.3.1	Evidence for the Freezing of the Transverse Component of the Spins.....	104
5.3.2	Evidence for the Freezing of the Longitudinal Component of the Spins .....	114
5.3.3	Signatures of the Spin-Glass Transitions in the Single-Crystal Neutron Diffraction Studies .....	119
5.3.4	The Outlook .....	127
5.4	Conclusions.....	131
<b>Chapter 6 Characteristics of the Spin-Glass Transitions Associated with Transverse and Longitudinal Freezing Using Polycrystalline Samples.....</b>		<b>133</b>
6.1	Introduction.....	133
6.2	Experimental.....	135
6.3	AC susceptibility $\chi(\omega, T, H, t)$ Studies on BaFe <sub>12</sub> O <sub>19</sub> .....	136
6.3.1	Comparison of $\chi(\omega, T)$ of Polycrystalline and Single-Crystalline Samples.....	136
6.3.2	Confirmation of Ergodicity Breaking for the two Transitions in BaFe <sub>12</sub> O <sub>19</sub> Powder .....	138
6.3.3	Evidence for the Gabay-Toulouse (G-T) and Almeida-Thouless (A-T) lines...	143
6.3.4	Evidence for the None-Exponential Relaxation: Isothermal Remanent Magnetization (IRM) .....	146
6.3.5	Study of Aging, Rejuvenation and Memory Effect in BaFe <sub>12</sub> O <sub>19</sub> .....	148
6.4	Conclusions.....	150
<b>Chapter 7 Role of Incommensurate Longitudinal Conical Modulation and Evidence for Another Spin-Glass Transition in BaFe<sub>12</sub>O<sub>19</sub>.....</b>		<b>153</b>
7.1	Introduction.....	153
7.2	Experimental.....	155
7.3	Results and Discussion .....	156
7.3.1	Evidence for a High-Temperature Diffuse Magnetic Transition: Magnetization and Specific Heat Studies .....	156
7.3.2	Signature of the Diffuse Magnetic Transition in Single-Crystal Neutron Diffraction Patterns .....	159
7.3.3	Confirmation of the Spin Glass Character of the Diffuse Magnetic Transition	165
7.4	Conclusions.....	173
<b>Chapter 8 Emergent Kagome Spin Configurations in the Basal Plane of BaFe<sub>12</sub>O<sub>19</sub> as a Function of Temperature .....</b>		<b>175</b>
8.1	Introduction.....	175
8.2	Experimental .....	176

8.3	Previous Predictions for Spin Canting in BaFe <sub>12</sub> O <sub>19</sub> .....	177
8.4	Neutron Powder Diffraction Studies.....	178
8.4.1	The Irreducible representation for Fe <sup>3+</sup> in BaFe <sub>12</sub> O <sub>19</sub> .....	180
8.4.2	Isotropy Subgroups for the Combination of Different Irreducible Representations .....	183
8.4.3	Details of the Rietveld Refinement.....	184
8.4.3.1	Results of Rietveld refinements.....	185
8.4.4	Evidence for Geometrical Frustration in the Magnetic Structure of BaFe <sub>12</sub> O <sub>19</sub> .....	187
8.5	Genesis of Randomness in BaFe <sub>12</sub> O <sub>19</sub> .....	192
8.5.1	Evidence for magnetoelastic strain in BaFe <sub>12</sub> O <sub>19</sub> .....	193
8.5.2	Role of the Exchange Anisotropy .....	199
8.5.3	The Origin of the Incommensurate Conical Spin-Glass Phase.....	200
8.6	Conclusions.....	202
<b>Chapter 9</b>	<b>Quantum Phase Transition in Ba<sub>(1-x)</sub>Ca<sub>x</sub>Fe<sub>12</sub>O<sub>19</sub>.....</b>	<b>205</b>
9.1	Introduction.....	205
9.2	Experimental.....	207
9.3	Results and Discussion .....	209
9.3.1	Evidence for chemical pressure generated by Ca <sup>2+</sup> substitution .....	209
9.3.2	Effect of Ca <sup>2+</sup> Substitution on Quantum Critical Behaviour of BFO .....	214
9.3.3	Evidence for Quantum Electric Dipole Glass State in Ca <sup>2+</sup> Substituted BFO... ..	218
9.3.4	Evidence for Quantum Electric Dipole Liquid (QEDL) Phase .....	221
9.4	Conclusions.....	227
<b>Chapter 10</b>	<b>Summary and Suggestions for Future Work .....</b>	<b>229</b>
10.1	Summary.....	229
10.2	Suggestions for Future work. ....	232
<b>References</b> .....		<b>235</b>
<b>List of Publications</b> .....		<b>293</b>

## List of Figures

Figure 1.1: Variation of magnetization and susceptibility below and above Curie temperature ( $T_c$ ) [38].	3
Figure 1.2: A few examples of Ising antiferromagnets [41].	4
Figure 1.3: Variation of susceptibility and inverse susceptibility of an antiferromagnetic materials [38]. AF: antiferromagnetic and P: paramagnetic.	5
Figure 1.4: Typical hysteresis loop for an antiferromagnetic material [46].	7
Figure 1.5: Variation of dielectric constant with temperature for a quantum paraelectric [49].	8
Figure 1.6: Schematic representation of magnetic spin in triangular lattice by considering (a) ferromagnetic and (b) antiferromagnetic nearest neighbour interactions [62].	9
Figure 1.7: Static (dc) susceptibility ( $M/H$ ) vs temperature ( $T$ ) plots of CuMn system with different magnetic impurity concentration (Mn) [61].	10
Figure 1.8: The temperature dependence of real part of ac-susceptibility of CuMn alloy system. Inset shows frequency dispersion across the freezing temperature. Peak position shifts to higher temperature side with increasing frequency [61].	11
Figure 1.9: Schematic representation of the temperature variations of the odd harmonics ( $\chi_1, \chi_3$ and $\chi_5$ ) in ac susceptibility [63].	12
Figure 1.10: Thermoremanent magnetization (TRM) plot of $\text{Ca}(\text{Fe}_{1/2}\text{Nb}_{1/2})\text{O}_3$ recorded at 15 K for 1000 Oe applied magnetic field using wait time of 1000 s [75].	13
Figure 1.11: Ternary phase diagram for the hexaferrites.	16
Figure 1.12: The arrangement of the different layers of $\text{O}^{2-}$ and $\text{Ba}^{2+}$ ion within the unit cell of $\text{BaFe}_{12}\text{O}_{19}$ M-type hexaferrite [98].	17
Figure 1.13: Unit cell of $\text{BaFe}_{12}\text{O}_{19}$ [98].	18
Figure 1.14: S, R and T blocks [12].	19

Figure 1.15: Schematic proposed magnetic structures of magnetoelectric Y-type hexaferrites. (a) collinearly ferrimagnetic [91], (b) the proper-screw [91] and (c) longitudinal-conical [101] magnetic structure. The short and long arrows indicate the effective moment in S and L blocks, respectively [91,101]. .....	21
Figure 1.16: Schematic (a) proposed transverse-conical [101] magnetic structures of Y-type hexaferrites and (b) cycloid type magnetic structure [91]. .....	22
Figure 1.17: Practical applications of hexagonal ferrites [12]. .....	24
Figure 1.18: Trigonal bipyramid polyhedra .....	25
Figure 1.19: Temperature dependence of reciprocal susceptibility of BaFe <sub>12</sub> O <sub>19</sub> single-crystal measured with dc field of 1000 Oe applied parallel (H // c) and perpendicular (H // ab) to the c-axis [137]. .....	28
Figure 1.20: (a) Variation of the magnetic viscosity <i>S</i> with temperature. Inset shows the behaviour of <i>S</i> on the zoomed scale [28]. (b) The c-axis dielectric permittivity $\epsilon_c$ as a function of temperature for BaFe <sub>12</sub> O <sub>19</sub> . Inset of (b) shows the same plot with a logarithmic scale in temperature [14]. .....	29
Figure 1.21: The $kT^{-1}$ versus $T^2$ plot in the lowest temperature region in the presence of 0 T and 14 T applied along c-axis. The inset shows the Arrhenius plot of $k^* = k - \beta T^3$ below ~125 mK [7]. .....	31
Figure 2.1: XRD profiles of BaFe <sub>12</sub> O <sub>19</sub> calcined at 1273 K and 1373 K. The position of impurity peak due to Fe <sub>2</sub> O <sub>3</sub> is marked with (*). .....	37
Figure 2.2: XRD profile for BaFe <sub>12</sub> O <sub>19</sub> , sintered at different temperatures. The position of the impurity peak of Fe <sub>2</sub> O <sub>3</sub> is marked with arrow. .....	38
Figure 2.3: (a) Image of the as-grown crystal and (b) Laue diffraction recorded on the single-crystal of BaFe <sub>12</sub> O <sub>19</sub> . .....	40



Figure 2.4: Comparison of XRD pattern on powder obtained after crushing the single-crystals and sintered samples of BaFe<sub>12</sub>O<sub>19</sub>. The arrow shows the position of the most intense peak of  $\alpha$ -Fe<sub>2</sub>O<sub>3</sub> which is absent in both the samples. ....40

Figure 2.5: Comparison of neutron powder diffraction (NPD) pattern collected on sintered samples with XRD pattern collected on powder obtained after crushing the single-crystals and sintered samples of BaFe<sub>12</sub>O<sub>19</sub>, at room temperature. The  $Q = 2.32 \text{ \AA}^{-1}$  marked with arrow is the position of most intense nuclear peak of  $\alpha$ -Fe<sub>2</sub>O<sub>3</sub> at 300 K. ....41

Figure 2.6: EDX spectra of single-crystal of BaFe<sub>12</sub>O<sub>19</sub>.....42

Figure 2.7: Observed (filled red circles), calculated (continuous black line), and difference (bottom green line) profiles obtained from Rietveld refinement using P6<sub>3</sub>/mmc space group for (a) powder and (b) single-crystal samples of BaFe<sub>12</sub>O<sub>19</sub>. The vertical bars (blue) represent the Bragg peak positions.....45

Figure 3.1: Schematic representation of (a) collinear magnetic structure of BaFe<sub>12</sub>O<sub>19</sub>, (b) coordination polyhedra for Fe<sup>3+</sup> ions in BaFe<sub>12</sub>O<sub>19</sub> and (c) longitudinal conical magnetic structure due to precession of the net moment in the R and R' blocks about the c-axis for canted spins.....51

Figure 3.2: XAS spectra of (a)  $\alpha$ -Fe<sub>2</sub>O<sub>3</sub>, GaFeO<sub>3</sub> and  $\gamma$ -Fe<sub>2</sub>O<sub>3</sub> [200,201], (b) LaFeO<sub>3</sub> [201], (c) Ba<sub>0.5</sub>Sr<sub>1.5</sub>Zn<sub>2</sub>Fe<sub>12</sub>O<sub>22</sub> [6] and (d) SrFe<sub>12</sub>O<sub>19</sub> [202] at the Fe L<sub>2,3</sub>-edges. 53

Figure 3.3: Atomic multiplet calculation based simulation of XAS spectra at the L<sub>2,3</sub>-edges of Fe at different Wyckoff position in SrFe<sub>12</sub>O<sub>19</sub> [202] with octahedral (OH), trigonal bipyramid (TBP) and tetrahedral (TH) environments. ....54

Figure 3.4 The Stoner model for the splitting of 3d valence band of transition metal in ferro/ferrimagnetic materials [205].....55

Figure 3.5: XMCD signal at the Fe L<sub>3,2</sub>-edges measured in the (a)  $\gamma$ -Fe<sub>2</sub>O<sub>3</sub> [206], (b) GaFeO<sub>3</sub> [200], (c) CoFe<sub>2</sub>O<sub>4</sub> [207] and (d) SrFe<sub>12</sub>O<sub>19</sub> [202]. OH, TPB and TH stand for octahedral, trigonal bipyramid and tetrahedral, respectively.....56

Figure 3.6: XMCD spectra at the Fe L<sub>2,3</sub>-edges calculated for each iron cation of SrFe<sub>12</sub>O<sub>19</sub> [202]. OH, TPB and TH stand for octahedral, trigonal bipyramid and tetrahedral, respectively.....58

Figure 3.7: (a) XAS spectra recorded at the Fe L<sub>2,3</sub>-edges measured at 1.2 K on a single-crystal of BaFe<sub>12</sub>O<sub>19</sub> in NI geometry using right ( $\sigma_+$ ) and left ( $\sigma_-$ ) circularly polarised X-ray beams. The dotted lines represent the linear background. (b) Normalised XAS spectra and (c) XMCD signal. OH and TH in (c) is stand for octahedral and tetrahedral environments.....62

Figure 3.8: (a) XAS spectra recorded at the Fe L<sub>2,3</sub>-edges measured at 1.2 K on a single-crystal of BaFe<sub>12</sub>O<sub>19</sub> in grazing incidence geometry without field using right ( $\sigma_+$ ) and left ( $\sigma_-$ ) circularly polarised X-ray beams. The dotted lines represent the linear background. (b) Normalised XAS spectra and (c) XMCD signal. ....64

Figure 3.9: (a) XAS spectra recorded at the Fe L<sub>2,3</sub>-edges measured at 1.2 K on a single-crystal of BaFe<sub>12</sub>O<sub>19</sub> in grazing incidence geometry with field of 0.5 T using right ( $\sigma_+$ ) and left ( $\sigma_-$ ) circularly polarised X-ray beams. The dotted lines represent the linear background. (b) Normalised XAS spectra and (c) XMCD signal. ....65

Figure 3.10: (a) The XMCD signal and (b) sum XAS along with their integration measured in grazing incidence geometry without field at 1.2 K. The dotted line in (b) is the two-step-like function used for edge jump removal before XAS integration.....66

Figure 3.11: (a) The XMCD signal and (b) sum XAS along with their integration measured in grazing incidence geometry with field of 0.5 T at 1.2 K. The dotted line in (b) is the two-step-like function used for edge jump removal before XAS integration. ...67

Figure 3.12: M-H curve measured at 2 K on single-crystal under various field applied (a) perpendicular and (b) parallel to the c-axis.....	68
Figure 3.13: Single-crystal neutron diffraction pattern recorded along $00l$ reciprocal lattice row at 1.5 K depicting a magnetic peak around $003$ position. The inset shows the triplet character of the magnetic peak with reflections at $l = 3$ and $l = 003 - \tau_1$ and $003 + \tau_2$ positions. ....	69
Figure 4.1: (a) Variation of the dc magnetization $M_{\perp c}$ and $M_{\parallel c}$ measured with a field of 500 Oe applied parallel ( $\parallel$ ) and perpendicular ( $\perp$ ) to the c-axis of the crystal. (b) The first derivative plot of $M_{\perp c}$ and $M_{\parallel c}$ with respect to the temperature. (c) Curie-Weiss fit for $\chi_{\parallel c}(T)$ and (d) $\chi_{\perp c}(T)$ .....	76
Figure 4.2: Magnified view of the temperature dependence of $M_{\perp c}$ and $M_{\parallel c}$ in the 2 K to 300 K range, measured with a dc field of 500 Oe, during the warming cycle on a ZFC crystal. The inset shows the occurrence of a magnetic transition at low temperatures on a magnified scale in a smaller temperature range.....	78
Figure 4.3: Variation of the magnetic anisotropy parameter $A = \left(\frac{M_{\perp c}}{M_{\parallel c}}\right)$ with temperature. Inset gives the magnified view in the vicinity of the transition temperature.....	78
Figure 4.4: XAS spectra and XMCD signals at the Fe $L_{2,3}$ -edges measured in the NI geometry without dc magnetic field bias measured at (a) 30 K, (b) 13.5 K, (c) 5.5 K and (d) 1.2 K. TH and OH in (a)-(d) stand for the tetrahedral and octahedral environments of Fe.....	81
Figure 4.5: XAS spectra and XMCD signals of Fe at the $L_{2,3}$ -edges measured in the GI geometry without dc magnetic field bias ( $H = 0$ T) at (a) 30 K, (b) 13.5 K, (c) 5.5 K and (d) 1.2 K. OH in (a)-(d) stands for octahedral environments of Fe. ....	82

Figure 4.6: XAS spectra and XMCD signals of Fe at the  $L_{2,3}$ -edges measured in the GI geometry with a biasing magnetic field of  $H = 0.5$  T at (a) 30 K, (b) 13.5 K, (c) 5.5 K and (d) 1.2 K. OH in (a)-(d) stand for octahedral environments of Fe. ....83

Figure 4.7: Comparison of the variation of the component of moments (a) longitudinal ( $M_{//c}$ ) and (b) transverse components ( $M_{\perp c}$ ) calculated using XAS, XMCD signal and dc magnetization measurements on the single-crystal. ....86

Figure 4.8: XAS spectra of oxygen at the K-edge recorded in normal incidence geometry at 1.2 K. ....89

Figure 4.9: Schematic representation of splitting of  $3dFe^{3+}$  orbitals in  $BaFe_{12}O_{19}$  due to crystal field and exchange-correlation effects at 1.2 K. ....90

Figure 4.10: (a) XAS spectra at the O K-edge recorded in the NI geometry at various temperatures. (b) XAS spectra on a zoomed scale. Peaks A1, A2, A3 and A4 in (b) are labelled as  $t_{2g}$ -bottom,  $t_{2g}$ -top,  $e_g$ -bottom and  $e_g$ -top, respectively. All the curves in (a) are shifted along the y-axis by 0.025. ....92

Figure 5.1: (a) Variation of the ZFC and FC magnetization ( $M_{\perp c}$ ) measured with dc field of 500 Oe applied perpendicular to the c-axis of the crystal. (b) Evolution of thermoremanent magnetization  $M_{\perp c}(t)$  of a 1000 Oe FC crystal with time at 40 K. (c) Temperature dependence of real  $\chi'_{\perp c}$  and imaginary  $\chi''_{\perp c}$  parts of the ac susceptibility measured at 545 Hz with an ac field drive of 3 Oe applied perpendicular to the c-axis of the crystal. ....105

Figure 5.2: Temperature dependence of (a) real  $\chi'_{\perp c}(\omega, T)$  and (b) imaginary  $\chi''_{\perp c}(\omega, T)$  parts of ac susceptibility measured at various frequencies using an ac drive field of 3 Oe applied perpendicular to c-axis of the crystal; (c) depicts the lower temperature anomaly in  $\chi''_{\perp c}(\omega, T)$  on a zoomed scale. The solid continuous lines through the data points in (c) are the fitted curves. ....108

Figure 5.3: Variation of the  $\ln(\tau)$  with  $1/T_f'$ . The continuous solid line through the data points is the result of the least-squares fit for Vogel-Fulcher law using  $\chi'(\omega, T)$  data.... 110

Figure 5.4: (a) Optimization of  $T_{SG}'$ . The minimum in (a) corresponds to the lowest variance with  $T_{SG}' \sim 46.035$  K. (b) The least-squares fit for the power-law for  $\ln(\tau)$  versus  $\ln((T_f' - T_{SG}')/T_{SG}')$  plot using  $\chi'(\omega, T)$  data..... 111

Figure 5.5: The  $\ln(\tau)$  vs  $1/T_f''$  plots for the (a) higher and (b) lower temperature transitions obtained from the  $\chi''_{\perp c}(\omega, T)$  data. The solid line is the least-squares fit for the Vogel-Fulcher law for the two transition with the best fit parameters given along with the figures. .... 112

Figure 5.6: Optimization of  $T_{SG}''$  for (a) the higher temperature and (b) the lower temperature transitions. The minimum in the two curves gives the optimised critical spin-glass transition temperatures which are indicated with an arrow in each figure. .... 113

Figure 5.7: The  $\ln(\tau)$  vs  $\ln((T_f'' - T_{SG}'')/T_{SG}'')$  plots for the power law type spin dynamics for the (a) higher and (b) lower temperature spin-glass transitions seen in  $\chi''_{\perp c}(\omega, T)$  data. The best fit parameters are listed along with the figures. .... 114

Figure 5.8: Temperature dependence of real  $\chi'_{//c}$  and imaginary  $\chi''_{//c}$  part of ac susceptibility measured at frequency 200 Hz using ac field of 3 Oe applied along the c-axis of the crystal. Inset shows the variation of  $\chi'_{//c}$  on the zoomed scale. .... 115

Figure 5.9: (a) Temperature dependence of the real  $\chi'_{//c}$  part of ac susceptibility measured at various frequencies using an ac drive field of 3 Oe applied parallel to the c-axis of the crystal. All the curves in (a) are shifted by  $0.012 \text{ emu/gOe} \times 10^{-2}$  along the y-axis and solid continuous line through the data points is a guide to the eyes. The  $\ln(\tau)$  versus  $1/T_f'$  plot for the two anomalies are shown in (b) for  $\sim 25$  K and (c) for  $\sim 15$  K transitions observed in  $\chi'_{//c}$ . The continuous solid line in (b) and (c) is least-squares fit for Vogel-Fulcher law..... 116

Figure 5.10: Optimization of $T'_{SG}$ for (a) higher and (b) lower temperature transition seen in Fig. 5.9(a).....	117
Figure 5.11: The $\ln(\tau)$ vs $\ln((T'_f - T'_{SG})/T'_{SG})$ plots along with the least-squares fit for the power law type spin dynamics for the (a) higher and (b) lower temperature transitions seen in $\chi'_{//c}(\omega, T)$ plots in Fig. 5.9(a). The best fit parameters are listed in the two figures. ....	118
Figure 5.12: Peak profile of $006$ Bragg reflection at (a) 1.5 K, (b) 10 K, (c) 50 K, (d) 100 K, (e) 200 K and (f) 300 K: The continuous solid lines through the data points (filled circles) are the fits for the back-to-back two exponential functions.....	121
Figure 5.13: Peak profile of $101$ Bragg reflection at (a) 1.5 K, (b) 10 K, (c) 50 K, (d) 100 K, (e) 200 K and (f) 300 K: The continuous solid lines through the data points (filled circles) are the fits for the back-to-back two exponential functions.....	121
Figure 5.14: Temperature dependence of the integrated intensity of $006$ Bragg reflection (a) on the full scale and (b) on the magnified scale, obtained from the neutron diffraction data collected on the single-crystal of $BaFe_{12}O_{19}$ . Broken lines in (a) and (b) are guide to the eyes, while the continuous solid line (black coloured) in (a) is the fit for the square of Brillouin function behaviour of $\mu$ . ....	122
Figure 5.15: Temperature dependence of the integrated intensity of $101$ Bragg reflection (a) on the full scale and (b) on the magnified scale, obtained from the neutron diffraction data collected on the single-crystal of $BaFe_{12}O_{19}$ . Broken lines in (a) and (b) are guide to the eyes, while the continuous solid line (black coloured) in (a) is the fit for the square of Brillouin function behaviour of $\mu$ . ....	123
Figure 5.16: Variation of $C_P$ with temperature (T).....	125
Figure 5.17: Variation of $C_P/T$ with square of the temperature (T).....	126
Figure 5.18: Variation of $C_P/T^3$ with temperature (T).....	127

Figure 6.1: Temperature dependence of  $\chi'_{//c}$  and  $\chi''_{//c}$  measured at 700 Hz with an ac field drive of 3 Oe applied (a) parallel ( $//$ ) to the c-axis and (b) perpendicular ( $\perp$ ) to the c-axis of the BFO crystals. This figure has been reproduced from chapter 5. (c) This figure depicts the real  $\chi'$  and imaginary  $\chi''$  parts of ac susceptibility measured at 700 Hz on powder samples at an ac drive field of 3 Oe. The continuous solid line through the data points (filled circles) is guide to the eyes. The dotted vertical lines indicate the first two transitions around 60 K and 25 K in the single-crystal sample. ....137

Figure 6.2: (a) The evolution of ac susceptibility measured on powder sample at (a) 200 Hz with different ac drive fields and (b) comparison of ac susceptibility measured at 50 Hz using ac drive field of 3 Oe and 13 Oe. Successive curves in (a) are shifted vertically by 0.0001 emu/gOe for clarity. The continuous solid line through the data points is guide to the eyes. ....138

Figure 6.3: Temperature dependence of the real part of ac susceptibility ( $\chi'(\omega, T)$ ) of the powder sample at various frequencies. Successive curves are shifted vertically by 0.00015 emu/gOe for clarity. The solid lines (wine coloured) are guide to the eyes. ....139

Figure 6.4: The  $\ln(\tau)$  versus  $1/T'_f$  plots for the (a) transverse and (b) longitudinal component of the spins. The continuous solid line through the data points is the Vogel-Fulcher fit..... 140

Figure 6.5: Optimization of the spin-glass transition temperature ( $T'_{SG}$ ) for (a) transverse and (b) longitudinal freezing..... 141

Figure 6.6: The  $\ln(\tau)$  vs  $\ln(T'_f - T'_{SG})/T'_{SG}$  plots for the freezing of the (a) transverse and (b) longitudinal components of the spins. The continuous line through the data points is the power-law fit..... 142

Figure 6.7: The  $\chi'(\omega=200\text{Hz}, T)$  plot for powder sample under different dc biasing magnetic field. The solid lines through the data points are guide to the eyes. .... 145

Figure 6.8: The T-H diagram showing the Gabay-Toulouse (G-T) with  $m = (2.0 \pm 0.04)$  and de Almeida-Thouless (A-T) with  $m = (0.65 \pm 0.001)$  lines. The continuous line through the data points in the T-H plane is the least-squares fit to the Equation (6.1) and (6.2)..... 145

Figure 6.9: Evolution of iso-thermoremanent ac susceptibility  $\chi'(\omega = 200\text{Hz})$  with time at (a) 40 K and (b) 10 K under 50 Oe dc biasing field. The solid lines (black coloured) through the data points in (a) and (b) are Kohlrausch-Williams-Watt (KWW) stretched exponential equation fits. .... 147

Figure 6.10: Evolution of isothermal remanent ac susceptibility  $\chi'(\omega=200\text{Hz})$  with time at (a) 40K and (b) 10K under 50 Oe dc biasing field measured with intermediate quenching to 35K and 5K, respectively. The solid lines (black coloured) though the data points in (a) and (b) are guide to the eyes. .... 150

Figure 7.1: Variation of magnetization with temperature measured for a BFO single-crystal for dc fields of (a) 500 Oe and (b) 1000 Oe applied parallel to the c-axis, and (c) 500 Oe applied perpendicular to the c-axis. The continuous line through the data points are guide to the eyes, whereas the dash-dot line in (c) shows the deviation from the linear behaviour of  $M_{\perp c}$  for  $200 < T < 300$  K. Panels (a) and (b) depict the results of both ZFC and FC measurements. Filled dots: FC and filled squares: ZFC. .... 157

Figure 7.2: (a) Variation of  $\chi'$  and  $\chi''$  with temperature measured at 700 Hz and 745 Hz for an ac drive field of 3 Oe applied (a) parallel and (b) perpendicular to the c-axis, respectively. The continuous lines through the data points are guide to the eyes while the dash-dotted lines for  $\chi''(T)$  curves depict departure from the linear trend below 200 K. The dashed-dotted line in  $\chi'_{//c}$  in (a) has been drawn to highlight the diffuse peak superimposed over the nearly linearly decreasing trend of the background value. .... 158



Figure 7.3:  $C_P/T$  versus  $T^2$  semi-log plot of  $BaFe_{12}O_{19}$  without any dc field bias. Inset shows the variation of  $C_P$  with temperature..... 159

Figure 7.4: Variation of the integrated intensity of (a)  $101$  and (b)  $006$  Bragg reflections with temperature. The continuous solid line shows the Brillouin fits for the integrated intensities unlike the plotted lines through the data points are guide to the eyes. .... 160

Figure 7.5: The evolution of the magnetic satellite peaks of BFO as a function of temperatures. The peak position of each satellite is marked with dotted lines. The continuous solid line through the data points is the deconvoluted profile..... 162

Figure 7.6: (a) The variation of the magnetic satellite peak positions,  $(003 - \tau_1)$  and  $(003 + \tau_2)$ , with temperature. (b) The variation of the integrated intensity of the magnetic satellite peak at  $(003 + \tau_2)$  position with temperature. The continuous solid lines are guide to the eyes. .... 163

Figure 7.7: (a) Variation of magnetization measured on zero-field cooled BFO powder at 100 Oe dc field. (b) Variation of  $\chi'$  and  $\chi''$  with temperature measured on BFO powder at 700 Hz with an ac drive field of 3 Oe. .... 166

Figure 7.8: (a) The variation of  $\chi''$  with temperature at 700 Hz. The continuous line below the peak in  $\chi''(T)$  is the fitted curve for modelling the rising background value of  $\chi''(T)$  above 100 K. The panel (b) depicts the rising background-subtracted peaks in  $\chi''(T)$  at various frequencies. .... 167

Figure 7.9: (a) Variation of  $\ln(\tau)$  versus  $1/T''_{SG}$  while the solid line is the least-squares fit for Vogel-Fulcher law. (b) Optimization of  $T_{SG}$  and (c) depicts the  $\ln(\tau)$  vs  $\ln((T''_f - T''_{SG})/T''_{SG})$  plot along with the fit to the power-law type spin dynamics for  $T_{SG} = 173.3$  K.... 168

Figure 7.10: Variation of the dc magnetization of the zero-field cooled powder samples of  $BaFe_{12}O_{19}$  measured during the warming cycle using a dc field of (a) 100 Oe, (b) 300 Oe, (c) 500 Oe, (d) 700 Oe, (e) 1000 Oe and (f) 1500 Oe. Arrows in (a)-(c) indicate the peak

position. Inset in (d) depicts the 1<sup>st</sup> derivative of magnetization in short temperature range.....170

Figure 7.11: The T-H diagram showing the Gabay-Toulouse (G-T) line. The continuous line through the data points in the T-H plane is the least-squares fit to the Equation (6.2) in chapter 6.....171

Figure 7.12: Evolution of iso-thermoremanent ac susceptibility  $\chi'(\omega = 200\text{Hz})$  with time measured at 100 K under 50 Oe dc biasing field. The solid lines through the data points is Kohlrausch-Williams-Watt (KWW) stretched exponential equation fit. ....171

Figure 7.13: Evolution of isothermal remanent ac susceptibility  $\chi'(\omega = 200\text{ Hz})$  with time measured at 100 K under 50 Oe dc biasing field measured with intermediate quenching to 95 K. The solid lines (black coloured) though the data points are guide to the eyes. ....172

Figure 8.1: Neutron powder diffraction patterns recorded at various temperatures. Inset shows a zoomed around the forbidden of  $003$  peak position. All the curves are shifted with respect to each other by 0.1 (arbitrary units). ....179

Figure 8.2: Isotropy subgroup tree for the magnetic space group  $P6_3/mm'c'$  .....184

Figure 8.3: The temperature variation of the (a)  $\chi^2$  and (b)  $R_M$ -factor obtained from the Rietveld analysis of neutron diffraction pattern collected at different temperatures. ....186

Figure 8.4: Observed (filled red circles), calculated (continuous black line), and difference (bottom green line) profiles obtained from the Rietveld refinement using neutron diffraction data at (a) 300K with  $\Gamma_{2a}$ , (b) 100K with  $\Gamma_{2(a \oplus b)}$ , (c) 50K with  $\Gamma_2 \oplus \Gamma_3$ , (d) 10K with  $\Gamma_2 \oplus \Gamma_3$  and (e) 10K with  $\Gamma_2 \oplus \Gamma_4$  for  $\text{BaFe}_{12}\text{O}_{19}$ . The vertical tick marks above the difference profile represent the Bragg peak positions (blue). ....188

Figure 8.5: Magnetic spin configurations obtained from Rietveld refinement of the magnetic structure using irrep  $\Gamma_{2(a \oplus b)}$  (a) longitudinal and (b) transverse components of the canted spins at 300 K and 250 K.....189

Figure 8.6: Magnetic spin configurations obtained from Rietveld refinement of the magnetic structure using irrep  $\Gamma_{2(a \oplus b)} \oplus \Gamma_3$ . (a) longitudinal and (b) transverse components of the canted spins at 100 K, 50 K and 10 K. .... 190

Figure 8.7: Kagome bilayer configuration linked via pyrochlore slabs [19]. .... 191

Figure 8.8: Observed (filled red circles), calculated (continuous black line), and difference (bottom green line) profiles obtained from Le-bail refinement using X-ray powder diffraction data at (a) 300 K, (b) 98 K, (c) 43 K (d) 23 K and (e) 13 K for  $\text{BaFe}_{12}\text{O}_{19}$ . The vertical tick marks above the difference profile represent the Bragg peak positions (blue). .... 194

Figure 8.9: The evolution of the lattice parameters (a) ‘a’ and (b) ‘c’ with temperature: filled red circle is from the XRD data. Filled squares (blue colour) are from NPD data discussed in the section 8.4.3.1. The solid black line is the straight-line fit. .... 195

Figure 8.10: Variation of the unit-cell volume with temperature: filled red circle is the XRD data, filled square (blue colour) is NPD data and solid black line is the fit for Debye Grüneisen equation. The broken line through the data points is the straight-line fit. .... 196

Figure 8.11: Variation of magnetization with dc magnetic field. .... 197

Figure 8.12: Variation of volume strain  $\omega_S$  (i.e.,  $\Delta V/V$ ) versus the square of spontaneous magnetization ( $M_S^2$ ) obtained from temperature-dependent M-H loop. .... 198

Figure 9.1: (a) Unit cell of M-Type hexaferrite. (b) Polyhedra of the M-type unit cell .. 210

Figure 9.2: (a) Observed (red circles), calculated (black continuous line) and difference (bottom green line) profiles obtained after Rietveld refinement using  $P6_3/mmc$  space group for  $\text{Ba}_{(1-x)}\text{Ca}_x\text{Fe}_{12}\text{O}_{19}$  with (a)  $x=0$ , (b)  $x=0.05$ , (c)  $x=0.07$  and (b)  $x=0.10$ . The vertical bars represent the Bragg peak positions (blue). .... 212

Figure 9.3: Variation of (a) lattice parameters  $a$ ,  $c$ , (b) unit cell volume  $V$  and (c) bond lengths Fe2-O1 and Fe2-O3 of  $\text{Ba}_{(1-x)}\text{Ca}_x\text{Fe}_{12}\text{O}_{19}$  in the composition range  $0 \leq x \leq 0.10$ .  
.....213

Figure 9.4: Variation of the real ( $\epsilon'$ ) and imaginary ( $\epsilon''$ ) parts of the dielectric permittivity of  $\text{Ba}_{(1-x)}\text{Ca}_x\text{Fe}_{12}\text{O}_{19}$  at 300 kHz for different  $\text{Ca}^{2+}$  concentrations with  $x =$  (a) 0, (b) 0.03, (c) 0.05, (d) 0.07 and (e) 0.10. Insets in (a)-(e) show the variation of  $\epsilon'$  on the zoomed scale.....215

Figure 9.5: Variation of ac susceptibility of BCFO- $x$ .....216

Figure 9.6: Variation of dielectric peak temperature ( $T_c$ ) at 300 kHz of  $\text{Ba}_{(1-x)}\text{Ca}_x\text{Fe}_{12}\text{O}_{19}$  as a function of  $\text{Ca}^{2+}$  concentration ( $x$ ). Inset shows variation of glass transition temperature ( $T_g$ ) as a function of  $\text{Ca}^{2+}$  concentration ( $x$ ). .....217

Figure 9.7: Variation of the real ( $\epsilon'$ ) part of the dielectric permittivity of  $\text{Ba}_{(1-x)}\text{Ca}_x\text{Fe}_{12}\text{O}_{19}$  for (a)  $x = 0$ , (b)  $x = 0.03$ , (c)  $x = 0.05$ , (d)  $x = 0.07$  and (e)  $x=0.10$  measured at various frequencies. ....219

Figure 9.8: Non-Arrhenius behaviour of temperature dependence of relaxation time ( $\tau$ ) shown in  $\ln(\tau)$  versus  $1/T$  plot of  $\text{Ba}_{(1-x)}\text{Ca}_x\text{Fe}_{12}\text{O}_{19}$  for (a)  $x=0.05$ , (b) 0.07 and (c) 0.10. The continuous line in insets (a)-(c) shows fit for  $\ln(\tau)$  vs  $\ln(T_{\text{max}} - T_g/T_g)$  plot using power law dynamics  $\tau = \tau_0(T_{\text{max}} - T_g/T_g)^{-z}$  characteristic of a dipolar glass transition.  
.....220

Figure 9.9: Curie-Weiss fit (black solid line) to temperature dependent permittivity (red circles) of  $\text{Ba}_{(1-x)}\text{Ca}_x\text{Fe}_{12}\text{O}_{19}$  for  $x =$  (a) 0.00, (b) 0.03, (c) 0.05 (d) 0.70 and (e) 0.10.....223

Figure 9.10: Variation of the magnitude of Curie-Weiss temperature  $|\Theta_{\text{cw}}|$  of  $\text{Ba}_{(1-x)}\text{Ca}_x\text{Fe}_{12}\text{O}_{19}$  with concentration ( $x$ ).....224

Figure 9.11: Specific heat of  $\text{BaFe}_{12}\text{O}_{19}$  as a function of temperature. Inset depicts the specific heat measured at different fields on a magnified scale.....224

Figure 9.12:  $C_p/T^{3/2}$  vs  $T^{3/2}$  plot where solid line represents the linear fit. Inset shows the non-Debye part of the specific heat at different magnetic fields. ....225

Figure 9.13: Boson peak at  $\sim 2.7$  K in  $\text{BaFe}_{12}\text{O}_{19}$  .....227



## List of Tables

Table 1.1: Chemical formula, sequences of S, R, and T blocks, and space groups for different type of hexaferrites [12].	15
Table 1.2: magnetic models for M-type hexagonal ferrites	27
Table 2.1: Average chemical composition of BaFe <sub>12</sub> O <sub>19</sub> in atomic wt% obtained from the EDX analysis.	42
Table 2.2: Asymmetric unit of the hexagonal phase of BaFe <sub>12</sub> O <sub>19</sub> in space groups P6 <sub>3</sub> /mmc.	44
Table 2.3: Positional coordinates, lattice parameters, and agreement factors obtained by Rietveld refinement using powder XRD data of BaFe <sub>12</sub> O <sub>19</sub> .	45
Table 2.4: Positional coordinates, lattice parameters, and agreement factors obtained by Rietveld refinement using single-crystal XRD data of BaFe <sub>12</sub> O <sub>19</sub>	46
Table 2.5: Comparison of our structural parameters with those reported in literature using single-crystal data.	46
Table 2.6: Interatomic distances (Å) obtained from Rietveld refinement powder XRD data of BaFe <sub>12</sub> O <sub>19</sub> .	47
Table 3.1: Energy of valleys and peaks in experimentally observed XMCD at the Fe L <sub>3</sub> -edge for SrFe <sub>12</sub> O <sub>19</sub> [202].	57
Table 3.2: Energy of valleys and peaks at the Fe L <sub>3</sub> -edge of calculated XMCD profiles of SrFe <sub>12</sub> O <sub>19</sub> [202].	59
Table 4.1: Energy of the valleys and peaks in the XMCD profile of Fe at the L <sub>3</sub> -edge measured in NI geometry with H = 0 T.	81
Table 4.2: Energy of valleys and peaks in the XMCD profile of Fe at the L <sub>3</sub> -edge measured in GI geometry with H = 0 T.	82

Table 4.3: Energy of valleys and peaks in the XMCD profile of Fe at the L <sub>3</sub> -edge measured in GI geometry with H = 0.5 T. ....	84
Table 4.4: Energy of the peaks t <sub>2g</sub> and e <sub>g</sub> bands observed at the O K-edge spectra recorded in NI geometry at various temperatures. ....	93
Table 4.5: Energy of the t <sub>2g</sub> and e <sub>g</sub> bands observed at the O K-edge spectrum recorded in NI geometry at various temperatures. ....	93
Table 4.6: Change in crystal field and exchange splitting energies with increase in temperature. ....	94
Table 5.1: List of parameters obtained after least-square fit to the Vogel-Fulcher and power-law dynamics to spin relaxation time. ....	128
Table 8.1: Basis vectors of the irreducible representation $\Gamma_n$ for magnetic ion (Fe <sup>3+</sup> ) named as Fe1 at 2a Wyckoff site with fractional coordinate (x=0, y=0, z=0) and Fe2 at 2(b) Wyckoff site with fractional coordinate (x=0, y=0, z=0.25). ....	181
Table 8.2: Basis vectors of the irreducible representation $\Gamma_n$ for magnetic ion Fe3 and Fe4 at 4f <sub>iv</sub> (4f1) site with fractional coordinate (x=1/3, y=2/3, z=0.0272) and at 4f <sub>vi</sub> (4f2) site with fractional coordinate (x=1/3, y=2/3, z=0.1904), respectively. ....	181
Table 8.3(a): Basis vectors of the irreducible representation $\Gamma_n$ for 6 out of 12 equivalent position of Fe5 at 12k site with fractional coordinate (x=0.168, y=2x, z=-0.1082). ....	182
Table 8.3(b): Basis vectors of the irreducible representation $\Gamma_n$ for the remaining six equivalent positions of Fe5 at the 12k site with fractional coordinate (x=0.168, y=2x, z=-0.1082). ....	183
Table 9.1: Atomic positions obtained from the Rietveld refinement for different compositions. ....	211



## List of Abbreviations

Antiferroelectric	AFE
Antiferromagnetic	AFM
BaFe <sub>12</sub> O <sub>19</sub>	BFO
Ba <sub>2</sub> Mg <sub>2</sub> Fe <sub>12</sub> O <sub>22</sub>	BMFO
Classical Phase Transitions	CPT
Energy Dispersive X-ray spectroscopy	EDX
Ferroelectric	FE
Ferromagnetic	FM
Grazing Incidence	GI
Irreducible Representations	Irreps
Isothermal Remanent Magnetization	IRM
Kohlrusch-Williams-Watt	KWW
Long-Range Ordered	LRO
Left Circularly Polarised	LCP
Magnetic Properties Measurement System	MPMS
Normal Incidence	NI
Neutron Powder Diffraction	NPD
Octahedral	OH
Physical Properties Measurement System	PPMS
Permanent Magnets	PM <sub>s</sub>
Right Circularly Polarised	RCP
Superparamagnetic	SPM
Scanning Electron Microscope	SEM

Synchrotron X-ray Diffraction	SXRD
Superconducting Quantum Interference Device	SQUID
Small- Angle Neutron Scattering	SANS
$\text{SrCr}_8\text{Ga}_4\text{O}_{19}$	SCGO
$\text{SrCr}_{9p}\text{Ga}_{12-9p}\text{O}_{19}$	SCGO-p
Spin-Glass	SG
Trigonal Bipyramid	TBP
Thermoremanent Magnetization	TRM
Tetrahedral	TH
Total Electron Yield	TEY
Quantum Phase Transitions	QPT
Quantum Critical Point	QCP
Quantum Electric Dipole Liquid State	QEDL
Quantum Paraelectricity	QPE
X-ray Powder Diffraction	XRD
X-ray Absorption Spectra	XAS
X-ray magnetic Circular Dichroism	XMCD
X-ray Magnetic Linear Dichroism	XMLD

## List of Symbols

Absorption Cross-Section	$\mu$
Angstrom	$\text{\AA}$
Anisotropy parameter	$A$
AC Susceptibility	$\chi(\omega, T)$
Activation Energy	$E_a$
Almeida-Thouless	A-T
Bohr Magnetron	$\mu_B$
Bifurcation/Irreversibility	$T_{\text{irr}}$
Bulk Modulus	$B$
Dzyaloshinskii-Moriya	D-M
Curie Constant	$C$
Curie Temperature	$T_c$
Curie-Wiess Temperature	$\Theta_{\text{CW}}$
Characteristic Relaxation Time	$\tau_0$
Critical Exponent.	$z\nu$
Critical Composition	$x_c$
Coercive Field	$H_c$
Dielectric Permittivity	$\epsilon'$
Debye Temperature	$\theta_D$
Electric Dipoles Density	$C'$
Exchange Interactions	$J$
Excitation Energy Gap	$\Delta$
Electron Volt	eV

Full-Width at Half-Maxima	FWHM
Frequency	$f$
Field Cooled	FC
Gabay-Toulouse	G-T
Grüneisen Parameter	$\gamma$
Intensity of Incident Electromagnetic Radiation	$I_0$
Intensity of the Beam After Passing Through the Sample	$I_t$
Kelvin	K
Longitudinal Component	//c
Transverse Component	$\perp c$
Neel Temperature	$T_N$
Paramagnetic	P
Propagation Vector	$\mathbf{k}$
Phase Shift	$\phi$
Magnetic Dipole Operator	$m_T^\theta$
Magnetic Field	H
Magnetization	M
Number of 3dFe <sup>3+</sup> holes	$n_h$
Remanent Magnetization	$M_r$
Stretched exponential function exponent	$\beta$
Specific Heat	$C_p$
Spin-Glass Transition Temperature	$T_{SG}$
Spin-Glass Freezing Temperature	$T_f$
Saturation Magnetization	$M_s$

Susceptibility	$\chi$
Spontaneous Electric Polarization	$P_s$
Thermal Parameters	B
Thickness	t
Unit Cell Volume	V
Vogel-Fulcher Freezing Temperature	$T_{VF}$
Wavelength	$\lambda$
Wait Time	$t_w$
Wait Temperature	$T_w$
XAS Spectra Measured using the RCP X-ray Beam	$\sigma_+$
XAS Spectra Measured using the LCP X-ray Beam	$\sigma_-$
XMCD Signal	$\Delta\sigma = (\sigma_+ - \sigma_-)$
Zero-Field Cooled	ZFC



## Preface

The study of phase transitions in frustrated magnetic systems has been a frontline area of research in solid-state and material sciences. The most commonly investigated source of frustration is frozen-in substitutional disorder leading to a competition between ferromagnetic (FM) and antiferromagnetic (AFM) interactions. Such a competition and randomness in certain situations can prevent the emergence of long-range ordered (LRO) phases and instead give rise to a unique spin-glass state in which the spins are randomly frozen below a frequency ( $\omega$ ) and field (H) dependent peak, usually called as spin-glass freezing temperature ( $T_f$ ), in the temperature dependence of magnetic susceptibility as a result of ergodic symmetry breaking. Frustration may also arise due to nearest neighbour AFM interactions alone due to the geometry of the lattice for spins arranged on the edge shared triangular (e.g.  $\text{YbZnGaO}_4$ ), corner shared triangular or kagome (e.g.  $(\text{H}_3\text{O})\text{Fe}_3(\text{SO}_4)_2(\text{OH})_6$  and  $\text{SrGa}_{12-x}\text{Cr}_x\text{O}_{19}$ ), pyrochlore (e.g.  $\text{Tb}_2\text{Mo}_2\text{O}_7$ ), and spinels (e.g.  $\text{MA}_2\text{O}_4$  with  $M = \text{Co}, \text{Fe}, \& \text{Mn}$ ) lattices. Such geometrically frustrated systems have evinced enormous attention in recent years as many of them exhibit exotic spin liquid, spin ice and spin-glass transitions even in the absence of any apparent site-disorder. Recent theoretical calculations seem to suggest that in the absence of any site-disorder, and hence randomness, the ground state of the geometrically frustrated systems has macroscopic degeneracy with no phase transition down to the absolute zero temperature. Such systems, however, have the possibility of the degeneracy getting lifted by quantum or thermal fluctuations through an intriguing mechanism known as “order by disorder” even in the absence of site disorder. More recent theoretical studies have shown that even an infinitesimal random disorder in the few body exchange interactions caused by anisotropic exchange interactions due to nearest neighbour bond length variations and/or magnetoelastic strains or dipole-dipole interactions between uncompensated spin or spin

clusters with intra-cluster geometrical frustration, can lift the degeneracy of the ground state and induce exotic phase transitions to spin liquid, spin glass and other complex ordered phases.

Frustration resulting from the geometry of the lattice considered so far in the literature is pre-existing in the paramagnetic high-temperature phase due to its crystal structure. In contrast to the pre-existing geometrical frustration, this thesis presents evidence for emergent geometrical frustration in the LRO phase of an M-type hexaferrite, namely  $\text{BaFe}_{12}\text{O}_{19}$  of immense commercial value worth about 4 billion dollars, at temperatures several hundred Kelvin below the ferrimagnetic transition temperature  $T_c \simeq 714$  K. Further, the genesis of the emergent geometrical frustration as well as its consequences on the low-temperature behaviour of LRO ferrimagnetic phase of  $\text{BaFe}_{12}\text{O}_{19}$  have been investigated in this thesis. A wide-ranging experimental techniques, involving X-ray absorption spectroscopy (XAS) and X-ray magnetic circular dichroism (XMCD) studies, X-ray and neutron powder diffraction studies, single-crystal neutron scattering studies, bulk magnetic susceptibility studies using both dc and ac fields on single crystals and powder samples, dielectric studies as a function of frequency and chemical pressure and specific heat studies on polycrystalline samples, have been employed in these investigations using in-house facilities as well as advanced synchrotron facility at Petra-III, DESY, Hamburg, FRM-II, Garching Germany and ISIS at Rutherford Appleton Laboratory, Harwell Oxford Didcot, UK, all as a function of temperature for  $T < 300$  K.

These studies have unravelled the complexity of the low-temperature phase transition behaviour of  $\text{BaFe}_{12}\text{O}_{19}$  and its ground state. The most significant finding of the present work includes the discovery of as many as five spin-glass transitions involving either the longitudinal or the transverse components of the spins or the precession



dynamics of the longitudinal conical magnetic structure in an ordered compound without any substitutional (site-) disorder and a quantum electric dipole glass state induced by a non-thermal variable. Presently, there no single theory that predicts a succession of five spin-glass transitions in a long-range ordered system with or without any substitutional site disorder. The present findings are expected to stimulate further theoretical and experimental studies in search of emergent geometrical frustration and its consequences in other hexaferrites as well as geometrically frustrated magnetic materials.

The present thesis comprises ten chapters, as outlined below briefly:

**Chapter 01** gives a brief introduction and a short review of the relevant literature on hexaferrites.

**Chapter 02** gives the details of  $\text{BaFe}_{12}\text{O}_{19}$  powder synthesis, sintering of these powders and crystal growth along with their characterization for phase purity and compositional stoichiometry.

**Chapter 03** presents evidence for the non-collinear magnetic structure of  $\text{BaFe}_{12}\text{O}_{19}$  in its ground state using XAS and XMCD studies at 1.2 K and discovery of incommensurate longitudinal conical modulation of the magnetic structure in single-crystal neutron diffraction studies in the ground state of  $\text{BaFe}_{12}\text{O}_{19}$ .

**Chapter 04** presents evidence for large magnetic anisotropy using dc magnetization studies in the 2 to 950 K temperature range with a peak around 45 K, canting of  $3d\text{Fe}^{3+}$  spins with respect to the c-axis using temperature and incident angle dependent XAS and XMCD studies at the Fe  $L_{2,3}$ -edges, splitting of the Fe-3d orbitals into  $e_g$  and  $t_{2g}$  bands due to crystal field effects and their further splitting due to exchange-correlations using XAS studies at the O K-edge and significant change in the exchange splitting around 15 K accompanied with change in the XMCD profile shapes and an upturn in dc magnetization perpendicular to the c-axis.

**Chapter 05** presents evidence for four successive spin-glass transitions in  $\text{BaFe}_{12}\text{O}_{19}$  single crystals whose spin dynamics diverges at  $T_{\text{SG}} \sim 46$  K,  $\sim 25$  K,  $\sim 15$  K and  $\sim 4$  K as per the Vogel-Fulcher and power-law fits for the spin relaxation time, anomalies in the temperature dependence of the specific heat in the  $C_p/T^3$  versus  $T$  and  $C_p/T$  versus  $T^2$  plots, diminution in the integrated intensities of the  $006$  and  $101$  reflections in single-crystal neutron diffraction studies around the spin-glass freezing temperatures and confirmation of the co-existence of the spin-glass phases with the long-range ordered ferrimagnetic phase of  $\text{BaFe}_{12}\text{O}_{19}$ .

**Chapter 06** investigates in detail various characteristics of the first set of longitudinal and transverse spin-glass phase transitions occurring at higher temperatures, using ac susceptibility studies on polycrystalline samples as a function of temperature, frequency, time, aging and magnetic field. These studies confirm ergodicity breaking at the two critical spin-glass transition temperatures, presence of Gabay-Toulouse (G-T) and Almeida-Thouless (A-T) lines in the T-H plane, non-exponential relaxation of isothermal magnetization and memory and rejuvenation effects below  $T_{\text{SG}}$ . These results are, surprisingly, in excellent agreement with the theoretically predicted T-H phase diagram for the disordered Heisenberg systems with negative single-ion anisotropy.

**Chapter 07** reports the discovery of another spin-glass transition in  $\text{BaFe}_{12}\text{O}_{19}$  as revealed by the divergence of the spin relaxation time at  $T_{\text{SG}} \sim 173$  K, field (H) dependent shift of the spin-glass freezing temperature  $T_f(\text{H})$  along the Gabay-Toulouse line, history-dependent irreversibility of  $M(T)$ , observation of non-exponential relaxation of the isothermal remanent magnetization as well as memory effects. Using high-resolution single-crystal neutron scattering studies, this chapter also presents evidence for longitudinal incommensurate conical modulation of the magnetic structure of  $\text{BaFe}_{12}\text{O}_{19}$  at all temperatures upto 300 K, except a narrow temperature range  $\sim 15$  K to  $\sim 35$  K,

where the modulation is commensurate. These studies reveal significant change in the integrated intensity of the satellite peaks and modulation wave vector across the spin-glass transition suggesting that this transition may be linked with the precession dynamics of the  $3d\text{Fe}^{3+}$  spins in the longitudinal conical magnetic structure of  $\text{BaFe}_{12}\text{O}_{19}$ .

**Chapter 08** presents arguments for the deviation from the collinear Gorter model, as confirmed in chapters 3 to 7, due to canting of the spins at the 12k Wyckoff sites of  $\text{BaFe}_{12}\text{O}_{19}$  unit cell, leaving the spins at the other sites aligned parallel or antiparallel to the c-axis as in the Gorter model. These arguments are used for the Rietveld analysis of the temperature-dependent neutron diffraction (NPD) patterns which reveal the emergence of fully frustrated kagome spin configuration as well as another kagome spin configuration with two-fold degeneracy as a function of temperature. Using temperature-dependent powder XRD studies, evidence for the presence of significant anisotropic magnetoelastic strains below 175 K with magneto-volume effect in different temperature ranges is also presented in this chapter. These magnetoelastic strains may provide the desired randomness to the few body exchange interactions in  $\text{BaFe}_{12}\text{O}_{19}$  required in the existing theories of spin-glass transition in geometrically frustrated ordered compounds.

**Chapter 09** presents the results of dielectric studies as a function of temperature and frequency from 1.66 K onwards to investigate the quantum critical behaviour of  $\text{BaFe}_{12}\text{O}_{19}$  involving electric dipoles. This chapter provides confirmation of quantum electric dipole liquid (QEDL) like state using dielectric and specific heat studies and reports the discovery of a new quantum electric dipole glass transition induced by a non-thermal variable which is chemical pressure in the present case.

**Chapter 10** summarizes the main finding of this thesis and list a few suggestions for future work.